



A reinforced energy-absorbing structure formed by combining multiple aluminum foam-filled open-hole tubes

Suchao Xie^{a,b,c}, Jing Zhang^{a,b,c}, Xiang Liu^{a,b,c,*}, Shiwei Zheng^{a,b,c}, Zinan Liu^{a,b,c}

^a Key Laboratory of Traffic Safety on Track (Central South University), Ministry of Education, Changsha, Hunan, China

^b Joint International Research Laboratory of Key Technology for Rail Traffic Safety, Changsha, Hunan, China

^c National and Local Joint Engineering Research Center of Safety Technology for Rail Vehicle, Changsha, Hunan, China

ARTICLE INFO

Keywords:

Open-hole tube
Aluminum foam
Crashworthiness
Multi-tube combination
Finite element analysis
Mechanical performance

ABSTRACT

In order to improve the energy absorption (EA) performance of thin-walled structures and overcome defects of a large peak impact force and large load fluctuation of multi-tube combined structures, the crashworthiness of aluminum foam-filled open-hole tubes (AFOTs) and their combined energy-absorbing structure was studied. Their EA performance was evaluated and effects of open-hole parameters including size, number and spacing of holes on axial compression characteristics were investigated through experiments and finite element analysis. The results indicate that the initiator of square holes can effectively reduce the initial peak crushing force (IPCF), but the reduced IPCF does not decrease exponentially with the increase of the number of holes, and the number and spacing of holes affect phases of wave crests and troughs on force–displacement curves. When at unequal spacings, the deformation mode of AFOTs changes in a sequence of extensional, mixed, and symmetric deformations with the increase in the spacing of the first hole. In view of wave crests and troughs with significant phase differences on force–displacement curves, a collaborative innovation combination mode based on AFOTs with different numbers and spacings of holes was proposed. A new, steady energy-absorbing structure, namely a structure combining four AFOTs, was developed by the combination of different numbers of tubes. In comparison with similar combined structures, the mean crushing force (MCF) is increased by 28.11% and the fluctuation in undulation of load-carrying capacity (ULC) is reduced by 66.09%.

1. Introduction

A thin-walled tube, as an efficient energy-absorbing element with a simple structure and controllable and ordered deformation [1–3], absorbs energy through plastic deformation to alleviate load when the tube is subjected to impact load [4,5]. Therefore, such a structure has been widely applied in transportation, aerospace, and mechanical engineering [6–8]. Under axial load, the crushing process of thin-walled structures has a certain limit, such as high initial peak force and an unstable mode of deformation. Under oblique load, the thin-walled structure is prone to overall bending resulting in a reduced energy absorption (EA) capacity. A crush initiator is considered as an effective method to produce reasonable deformation and improve EA characteristics. Structural modifications such as use of a groove [9–12], different shapes of holes [13–15], and geometrical designs based on paper folding [16–18] are some examples of crush initiators used in such devices.

The axial and oblique crashworthiness of thin-walled structures

without crush initiators has been extensively studied in the field of transportation [19,20]. Abramowicz and Jones [21,22] assessed the axial crushing performance of thin-walled tubes and developed a theoretical model of the mean crushing force (MCF) considering strain strengthening, strain rate of materials, and effective deformation distance. Liu et al. [23] experimentally and numerically investigated the effects of the temperature and strain rate on plastic deformation behaviors of tubes and established a prediction model for crushing of tubes. Moreover, thin-walled structures with different cross-sectional shapes have been studied, such as circles [24], quadrilaterals [25], hexagons [26], octagonal [27], and concave tubes [28]. To satisfy application requirements of thin-walled structures in various settings, many researchers have performed crashworthiness design and optimized objectives with methods, such as genetic algorithms and neural networks [29], multi-objective particle swarm optimization algorithms [30,31] and genetic algorithms [32]. Bahramian and Khalkhali [33] conducted topological optimization of crashworthiness of thin-walled tubes using an improved bi-directional evolutionary structure.

* Corresponding author at: Key Laboratory of Traffic Safety on Track (Central South University), Ministry of Education, Changsha, Hunan, China.

E-mail address: xiangliu06@gmail.com (X. Liu).

Nomenclature

EA	energy absorption
AFOT	aluminum foam-filled open-hole tube
ULC	undulation of load-carrying capacity
PCF	peak crushing force
IPCF	initial peak crushing force
CFE	crushing force efficiency
SEA	specific energy absorption
OT	open-hole tube
b	the side-length of the square tube
c	the side-length of the aluminum foam
N	the number of holes
ΔL_n	equal hole spacing
$\Delta L_n'$	unequal hole spacing
Two-AFOTs	two-AFOT combined structure
Three-AFOTs	three-AFOT combined structure
Four-AFOTs	four-AFOT combined structure
AFT	aluminum foam-filled tube

Baykasoğlu et al. [34] designed a lattice structure filled thin-walled tube and optimized objectives of minimizing peak crushing force (PCF) and maximizing specific energy absorption (SEA) through weighted superposition attraction and an artificial neural network. Patel et al. [35] optimized a thin-walled multi-layer structure based on gray relation analysis and found that a three-layer configuration confers better crashworthiness.

Although thin-walled structures without crushing initiators demonstrate good EA capacity under axial load, such structures yield high magnitude of the initial peak force and unstable deformation response, therefore, many scholars have added a crush initiator with auxiliary deformation properties onto thin-walled structures to improve the stable deformation capacity. Crush initiator guides the tubes to produce controllable deformation and reduces the initial peak crushing force (IPCF) of the structure, thus improving the crashworthiness of the structure. Cho et al. [36] studied thin-walled tubes with grooves through numerical simulation to estimate influences of the ratio of thickness to width on the crashworthiness of thin-walled structures. Based on experiments [37] and numerical simulations [38], Bodlani et al. investigated effects of circular holes on EA performance of thin-walled tubes. The results show that circular holes introduced within a certain range can reduce the IPCF and improve the EA capacity of thin-walled tubes. Li et al. [39] and Kathiresan [40] studied different types and numbers of crush initiators into thin-walled tubes and found that a reasonable number of crush initiators can improve the crashworthiness of structures. Kim et al. [41] investigated effects of design parameters for thin-walled tubes with holes through finite element model and design of experiments. Their research indicated that circular holes in a hexagonal array are most effective in increasing the crushing energy. The aforementioned studies have shown that the axial compression characteristics of thin-walled structures depend on the number, shape, and size of crush initiators.

In addition to adding a crush initiator, filling functional materials in tubes is also a method used to reduce the possibility of the global buckling. To overcome the defect and fully exploit spatial resources in tubes [42], many researchers improved the deformation stability and energy dissipation capacity of thin-walled structures by infilling with functional materials. The porous materials represented by metal foam exhibit good crashworthiness [43–46], so scholars have begun to focus on filling structures of thin-walled tubes. The filled structures combining metal thin-walled structures with foam improve the overall stability of structures due to addition of energy-absorbing materials. Furthermore, the overall bearing capacity and EA performance of filled structures are

improved due to the interaction between foam and thin-walled tubes [47–49]. Seitzberger et al. [50] studied single tubes, two tubes, hollow tubes, and aluminum foam-filled tubes (AFTs) with different materials, sizes, and cross-sectional shapes and found that filling with aluminum foam can improve the EA of tubes. By using a non-linear finite element model, Ahmad and Thambiratnam [51] assessed EA performance and axial crushing performance of aluminum foam-filled tapered tubes under quasi-static compression. They also found the effects of relevant parameters, such as density of aluminum foam, wall thickness, and half-cone angle on structures. Wang et al. [52] investigated foam-filled tubes with three average particle sizes under quasi-static axial compression and analyzed effects of parameters, such as ratio of radius to thickness and ratio of height to diameter on deformation mechanisms, mechanical properties, and EA capacity of foam-filled tubes. Moreover, they established a formula for mean crushing force of the three structures. Liu et al. [53] experimentally and theoretically studied mechanical responses and EA of different shapes of aluminum foam-filled tubes and hollow tubes. Song et al. [54], Gong et al. [55], Xiang et al. [56] and Yao et al. [57] designed a new aluminum foam-filled structure inspired by plant and animal structure and found that the EA capacity of a bionic structure is higher than that of a corresponding fully filled specimen.

The aforementioned research is studied from the perspective of the single tube. The speed of the high-speed train continues to increase, and the crashworthiness requirements of energy-absorbing structures are also improved. To improve the crashworthiness of thin-walled structure in a limited space, the researchers proposed a thin-walled combination structure. Haghi Kashaniet al. [58] studied parallel and diamond arrangements for double-tube arrangements. The results show that absorbed energy by bi-tubular systems is more than the sum of the energy by inner and outer tubes loaded separately, and diamond arrangement allows greater EA than the parallel arrangement. Azimi and Asgari [59] and Goel [60] investigated that the foam-filled bi-tubular tubes could improve its EA under axial and oblique loads. Sharifi et al. [61] studied different parameters including diameter, wall-thickness of each tube, and the interaction between two tubes. The results show that the crashworthiness of double tubular composite structure was better than that of single tubes. Patel et al. [35] studied the crash-response of double, triple, and four layered frusta; the results show that triple layered frusta were found to have better performance among all studied structures. Other scholars studied the crashworthiness of single tubes and double tube combination [62], but few have studied three-tube and multi-tube combinations in such systems.

Some scholars have studied influences of a crush initiator on the EA performance of thin-walled structures and reached conclusions with reference value, the studies are based on hollow thin-walled structures. With the improvement of standards for the safe collision speed, conventional thin-walled metal energy-absorbing elements cannot meet energy consumption requirements under a higher standard applied to the safe collision speed. Compared with conventional thin-walled tubes, aluminum foam-filled tubes with crush initiators demonstrate certain advantages in deformation modes and EA performance. The spacing between crush initiators is used to control the collapse sequence of filled structures and the defects of the high IPCF and large load fluctuation in existing multi-tube combinations are overcome through filled multi-tube structures combined in different sequences.

Materials and methods are introduced in Section 2, including details of the finite element model and the results of the validation of the structure. Section 3 covers the parameters (including the size, equal distance and unequal distance of hole) and their influences on the crashworthiness of the aluminum foam-filled open-hole tube (AFOT). The force-displacement curves and crashworthiness indicators were also analyzed. The combination of AFOTs with the best properties was then studied to reduce load fluctuations and enhance the EA stability of structures. An efficient and stable four-AFOT combined structure was obtained, which is expected to be used in the design of such energy-absorbing buffer devices in high-speed trains.

2. Materials and methods

Experimental structure and numerical simulation method will be studied and crashworthiness indicators are introduced to assess the axial compression characteristics.

2.1. Crashworthiness indicators

The crashworthiness of thin-walled structures is often evaluated using appropriate indicators. Generally, indicators, such as EA, SEA, IPCF, MCF, crushing force efficiency (CFE), and undulation of load-carrying capacity (ULC) are introduced to assess the crashworthiness of structures [63,64].

(1) EA

EA represents the total energy absorbed in the deformation process, which can be obtained by the integration of a force–displacement curve, expressed as follows:

$$EA(d) = \int_0^d F(x) dx \quad (1)$$

where, $F(x)$ and d denote the force in the compression process and compression distance, respectively.

(1) SEA

SEA stands for the energy absorbed per unit mass during axial compression, which is expressed as follows:

$$SEA = \frac{EA(d)}{M} \quad (2)$$

where, M denotes the total mass of the structure. According to Formula (2), for a structure with high SEA, lowering its mass when ensuring safety under collision conditions can meet design requirements related to light-weighting and energy saving, moreover, the EA of the structure is higher.

(1) IPCF

IPCF refers to the maximum value reached when buckling begins during axial compression.

(1) MCF

MCF is the arithmetic mean value on the force–displacement curve in the axial compression process, which is expressed as follows:

$$MCF = \frac{EA(d)}{d} \quad (3)$$

(1) CFE

CFE represents the ratio of the MCF to the IPCF as given by:

$$CFE = \frac{MCF}{IPCF} \quad (4)$$

For the energy-absorbing structure, the higher the CFE is, namely the closer the MCF to the peak crushing force is, the higher the effective rate of utilization of the materials.

(1) ULC

ULC is the fluctuation of the force–displacement curve and charac-

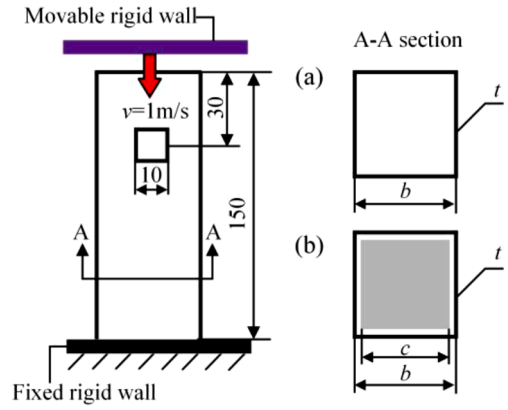


Fig. 1. Dimensions, force, and boundary conditions of the OT and AFOT under axial compression at a crushing speed of 1 m/s: (a) Top view of OT; (b) Top view of AFOT and aluminum foam (unit: mm).

terizes the distance of crushing force from the MCF, which is expressed as:

$$ULC = \frac{1}{EA} \int_0^d |F(x) - MCF| dx \quad (5)$$

The smaller the ULC, the smoother the force–displacement curve, the closer the crushing force is to a constant and the higher the overall stability of the energy-absorbing structure.

2.2. Finite element model of the structure

Quasi-static axial compression of the structure was numerically simulated by using the finite element explicit software LS-DYNA [65]. An open-hole tube (OT) with length L of 150 mm, width b of 50 mm, thickness t of 2 mm, and a side-length of the aluminum foam c of 40 mm is shown in Fig. 1. The crushing initiators are same square holes set on two opposite sides of the tube. The OT is divided into four-noded Belytschko–Tsay shell elements (referred to herein as the BT algorithm). The BT algorithm uses single point integration and has the advantage of rapidity of calculation. To capture more deformation behaviors in the axial crushing deformation process, five integration points were set in the thickness direction. Such an element is suitable for the simulation of large structural deformation and has been adopted in previous studies on EA. A piece-wise linearly plastic material (MAT_24 in LS-DYNA) is used to model the OT and AFOT. The MAT_24 constitutive model is an elastic-plastic material model, which is most widely used and applicable to most metal materials. A rigid material (MAT_20 in LS-DYNA) was used in the upper and lower rigid walls. Parts made from this material are considered to be rigid. Many foam constitutive models have been integrated in HyperMesh, so the macro modeling method is adopted. Aluminum foam was modeled by eight-node hexahedrons and solid elements were defined by *SECTION_SOLID by combining integral technology and hourglass control. A ‘Constant stress solid element (default element type)’ integral scheme was adopted, and crushable foam materials (MAT_63 in LS-DYNA) were selected. The MAT_63 constitutive model is a foam model with crushing properties, which is suitable for the modeling of aluminum foam material. The material setting unloading is a completely ideal elastic process. The stress–volumetric strain curve was replaced by inputting the stress–compressive strain curve. The bottom of the tube was fixed, while the top was axially compressed by the upper rigid wall. The crushing speed was 1 m/s, as shown in Fig. 2. The 6063-T5 aluminum alloy was insensitive to strain rate [66,67], so the influence of strain rate was ignored in this numerical simulation.

To study the convergence of the grid, sensitivity analysis was

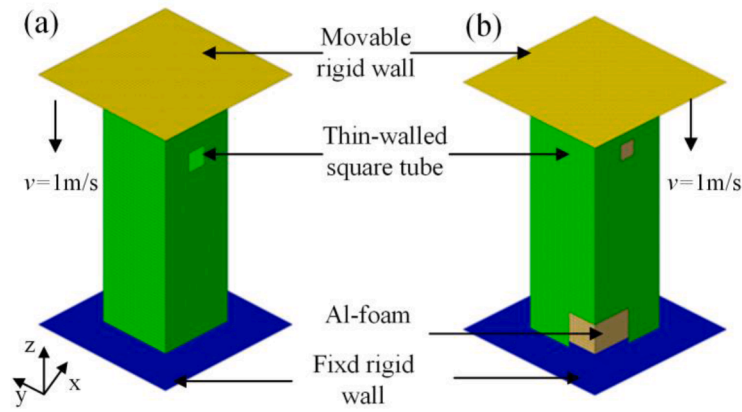


Fig. 2. Finite element model of the OT and AFOT consistent with experimental conditions under axial compression at a crushing speed of 1 m/s: (a) The finite element of OT; (b) The finite element of AFOT.

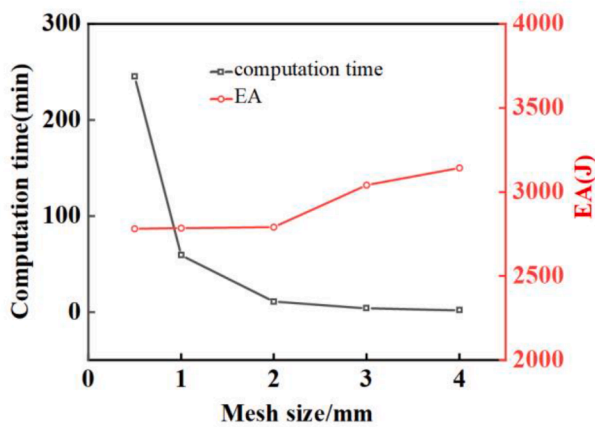


Fig. 3. Mesh sensitivity analysis for the test OT between computation time and EA, and the red line represents EA and the black line represents computation time.

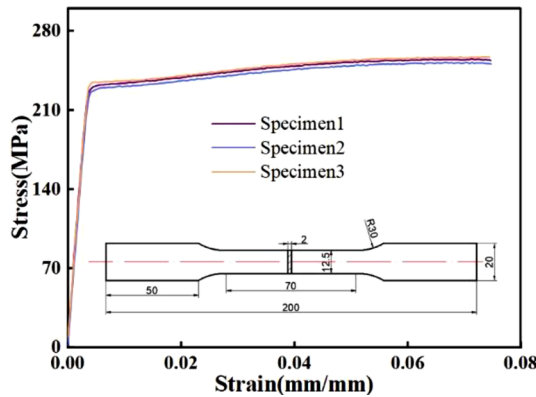


Fig. 4. True stress-strain curves of three specimens made of the AA6063-T5 materials and the dimensions of AA6063-T5 tensile specimens.

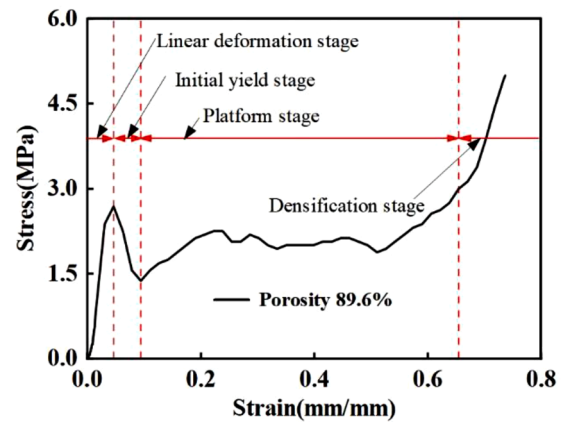


Fig. 5. Stress-strain curve of aluminum foam with a density of 0.28 g/cm^3 with four stages: linear deformation stage, initial yield stage, platform stage, and densification stage.

conducted on the grid size of OT, as shown in Fig. 3. It was found that an element size of $2 \text{ mm} \times 2 \text{ mm}$ can ensure the accuracy of the numerical simulation and limit the increase of computation time. Similarly, the solid element can maintain the same convergence at a grid measuring $4 \text{ mm} \times 4 \text{ mm}$.

During axial compression of the OT and the AFOT, the contact of the end face of the thin-walled tube with the movable and fixed rigid walls was defined by *CONTACT_AUTOMATIC_NODES_TO_SURFACE. The contact between the OT or aluminum foam itself was defined through *CONTACT_AUTOMATIC_SINGLE_SURFACE. The contact of aluminum foam with both the movable and fixed rigid walls as well as contact between the OT and aluminum foam could be defined based on *CONTACT_AUTOMATIC_SURFACE_TO_SURFACE. The dynamic and static friction coefficients were set to 0.25 and 0.3 [68].

2.3. Materials and properties

AA6063-T5 materials were used for tubes and mechanical properties were measured using an MTS 322T hydraulic material testing machine, at a loading rate of 2 mm/min . The dimensions of specimens made of the

Table 1
Mechanical parameters of the AA6063-T5 materials.

Parameters	Density ρ (kg/cm^3)	Young's modulus E (GPa)	Poisson's ratio μ	Yield stress σ_y (MPa)	Limiting stress σ_u (MPa)	Ultimate tensile strain ϵ_u
values	2700	70	0.3	228.81	252.78	0.075

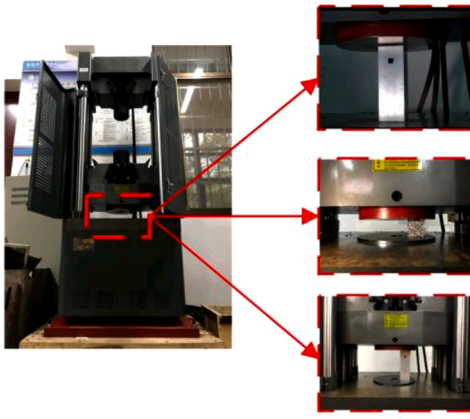


Fig. 6. WED-600 electro-hydraulic servo-controlled universal testing machine for OT, aluminum foam and AFOT under axial compression at a crushing speed of 10 mm/min.

materials and stress-strain curves obtained through experiments with Chinese Standard GB/T 228.1–2010 [69] are shown in Fig. 4 and mechanical parameters are listed in Table 1.

Aluminum foam specimens were prepared by wire cutting, with the main hole size ranging between 2.5 mm and 5 mm. Aluminum foam with the density of 0.28 g/cm³ was selected as a filling material (porosity of 89.6%). The stress-strain curve in Fig. 5 was obtained through a quasi-static compression test. The stress-strain curve of aluminum foam can be divided into four stages: (1) linear deformation stage; (2) initial yield stage; (3) platform stage; (4) densification stage.

2.4. Verification of finite element model

The quasi-static axial compression tests of the OT, aluminum foam and AFOTs were conducted with a WED-600 electro-hydraulic servo universal testing machine, as shown in Fig. 6. The measurement range was 600 kN and axial loading velocity was set to 10 mm/min. The force-displacement curves in Fig. 7 and axial crushing deformation diagrams were obtained by comparing experimental results with simulation results.

Fig. 7(a) shows that the experimental and simulation curves of OTs follow similar trends, and wave peaks and troughs are in good

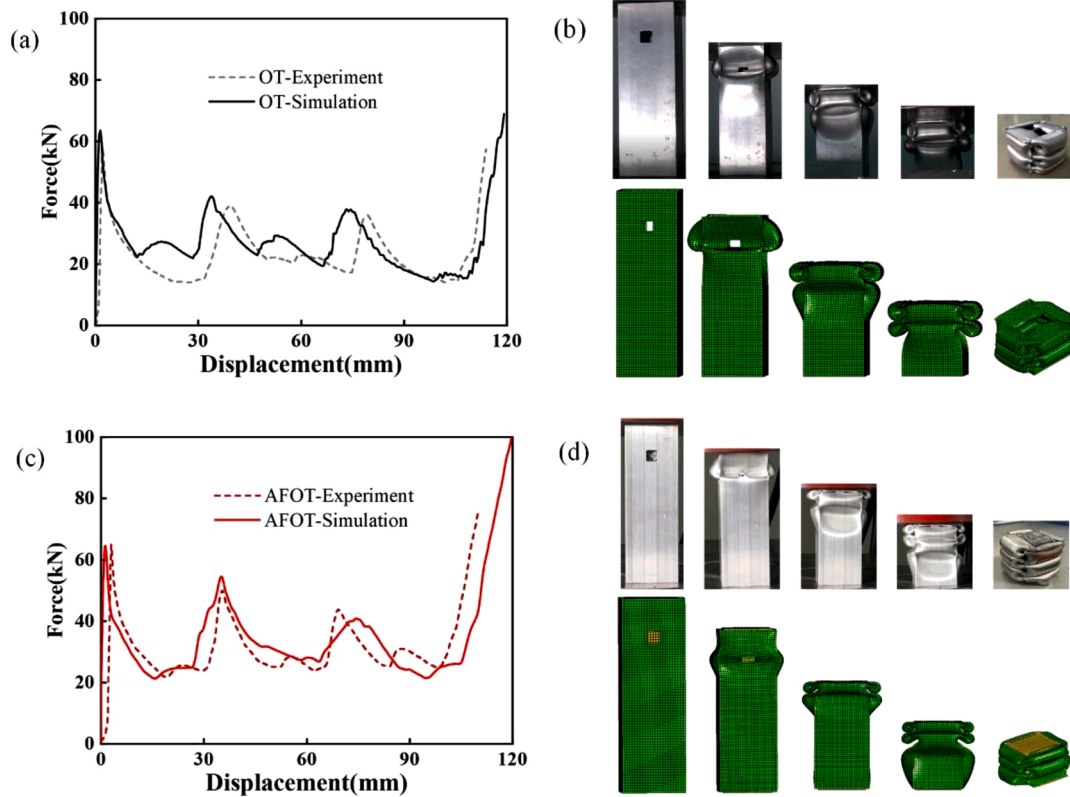


Fig. 7. Comparison between experimental results and finite element simulation: (a) Force-displacement curves of OTs; (b) Diagram of OT deformation process at different heights; (c) Force-displacement curves of AFOTs; (d) Diagram of AFOT deformation process at different heights.

Table 2

Comparison of the experimental and FE simulation results.

Structure	Type	EA(J)	M(g)	SEA(J/g)	IPCF(KN)	MCF(KN)	CFE(%)
Open-hole tube	Experiment	2578	148.6	17.35	58.40	23.44	40.14
	Simulation	2791	148.6	18.78	64.54	25.37	39.31
	Error	8.3%	0	8.2%	10.5%	8.2%	2.1%
Aluminum foam-filled open-hole tube	Experiment	3443	203.8	16.89	64.9	31.30	48.23
	Simulation	3504	203.8	17.19	64.56	31.85	49.33
	Error	1.8%	0	1.8%	0.5%	1.8%	2.3%

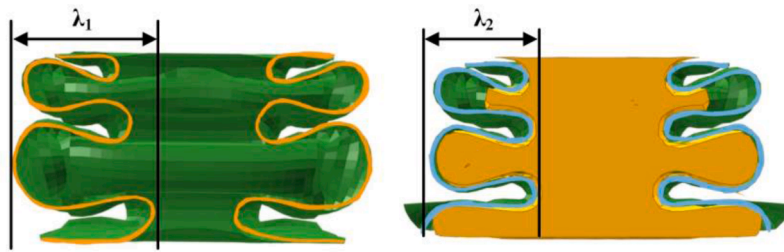


Fig. 8. Cross-sectional view of the OT and AFOT in the numerical simulations with the measurement result of $\lambda_1 = 29.868mm$ and $\lambda_2 = 22.270mm$ for the folded flap of OT and AFOT.

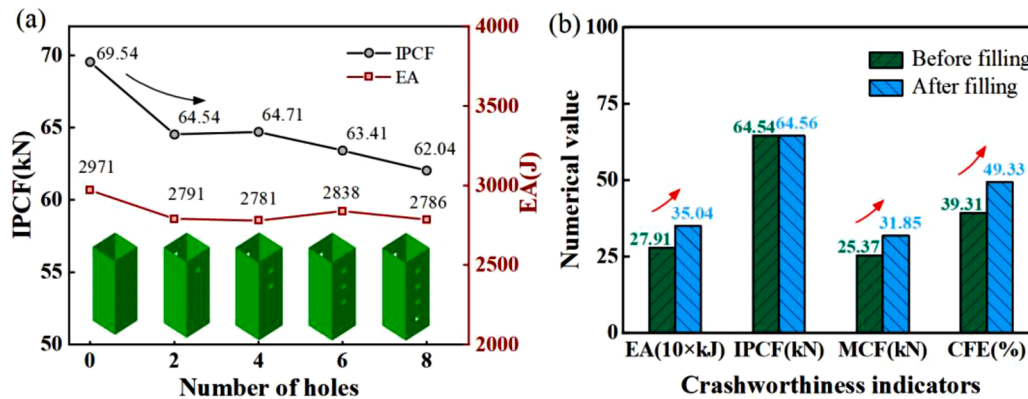


Fig. 9. Advantages of the AFOT structure: (a) Changes of IPCF and EA after adding open-hole structures; (b) Comparison of crashworthiness including EA, IPCF, MCF, and CFE performance after filling with aluminum foam.

agreement. Meanwhile, Fig. 7(b) shows the deformation process diagram of OT. Three folds are formed in both experiment and simulation, corresponding to three peaks and troughs on force-displacement curve,

which is consistent with the conclusion of Abramowicz and Jones [22]. By analyzing force-displacement curve, the comparison of crashworthiness indicators is summarized in Table 2. For instance, the EA

Table 3
Three deformation modes of the AFOT.

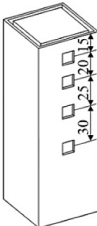
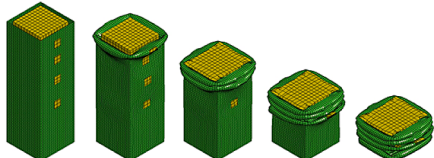

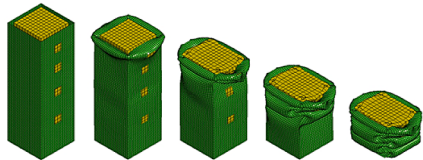
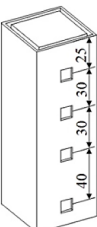
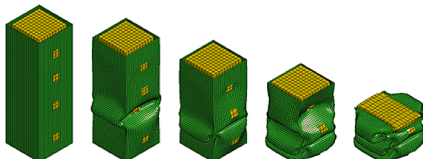
Size	Deformation process	Deformation mode
		(a) Extensional mode
		(b) Mixed mode
		(c) Symmetric mode

Table 4

Crashworthiness indicators of AFOTs with different sizes of square holes.

$b \times b (\text{mm}^2)$	EA (J)	SEA (J/g)	IPCF (kN)	MCF (kN)	CFE (%)
6×6	3516	17.19	67.32	31.96	47.47
8×8	3528	17.28	66.03	32.07	48.57
10×10	3504	17.19	64.56	31.85	49.33
12×12	3426	16.84	62.85	31.15	49.56

obtained in the finite element simulation is 8.2% greater than the experimental value, and the difference in the CFE value is somewhat smaller at a difference of 2.1%. These differences may be due to a variety of reasons: manufacturing error, experimental complexity, etc. Similarly, the experimental and simulation comparison of the AFOT is shown in Fig. 7(c) and (d). The difference in the crashworthiness indicators between experiment and simulation is less than 11%, therefore, the finite element model employed appears to be valid and can be used to assess the crushing performance of the OT and AFOT. Meanwhile, the deformation process obtained via the simulation does match that found in the experiment; this also validates the accuracy of the finite element model.

The number of folded lobes in the AFOT structure increases from five to six, namely the fold wavelength of the structure reduces. In the meanwhile, the densification stage of the structure occurs earlier. A cross-sectional view is shown in Fig. 8 and the measurement result is $\lambda_1 = 29.868\text{mm} > \lambda_2 = 22.270\text{mm}$. This is because the coupling between aluminum foam and thin-walled tubes reduces inward folding of thin-walled tubes and fold wavelength in the bulking of the tube wall, so more folds are formed under axial compression [70,71].

The axial crushing deformation of structures shows that collapse of structures preferentially occurs at holes. The numerical simulation results of structures without holes and with different numbers (2, 4, 6, and 8) of square holes were compared. As illustrated in Fig. 9(a), with the

increase in the number of square holes, the IPCF of the structure constantly decreases and the EA reduces. The reduced IPCF does not decrease exponentially with the increase in the number of holes. Therefore, it represents that the axial crush performance of thin-walled tubes is strongly dependent on the number of initiators, a surfeit of initiators can impair the performance. To make up for structural defects caused by holes and make full use of the space of tubes, tubes were filled with aluminum foam. Crashworthiness indicators were compared before and after filling tubes with two holes in Fig. 9(b). The EA, MCF, and CFE of the filled structure increase where EA increases from 2791 J to 3504 J. Aluminum foam plays an important role in enhancing EA and improving the deformation stability of OTs.

Under quasi-static axial load, Table 3 shows three different deformation modes, namely extensional deformation mode (a), symmetric deformation mode (b) and mixed-deformation mode (c) of the thin-walled AFOT under different spacings of holes. The deformation mode of the AFOT changes with the gradual increase of the spacing between holes under the same number of holes. When extensional modes of deformation occur, all four edges fold inward or outward. When symmetric deformation occurs, two opposite sides are folded outward, and the other two are folded inward (the mixed mode lies between these two cases).

3. Results and analysis

To evaluate the effects of hole parameters, the mechanisms of influence of the size, number, and spacing of square holes on axial compression characteristics and deformation behaviors of AFOTs were studied.

3.1. Effects of hole size

Firstly, the hole size was determined. On the AFOT structure with two square holes, square holes with sizes of 6×6 , 8×8 , 10×10 , and

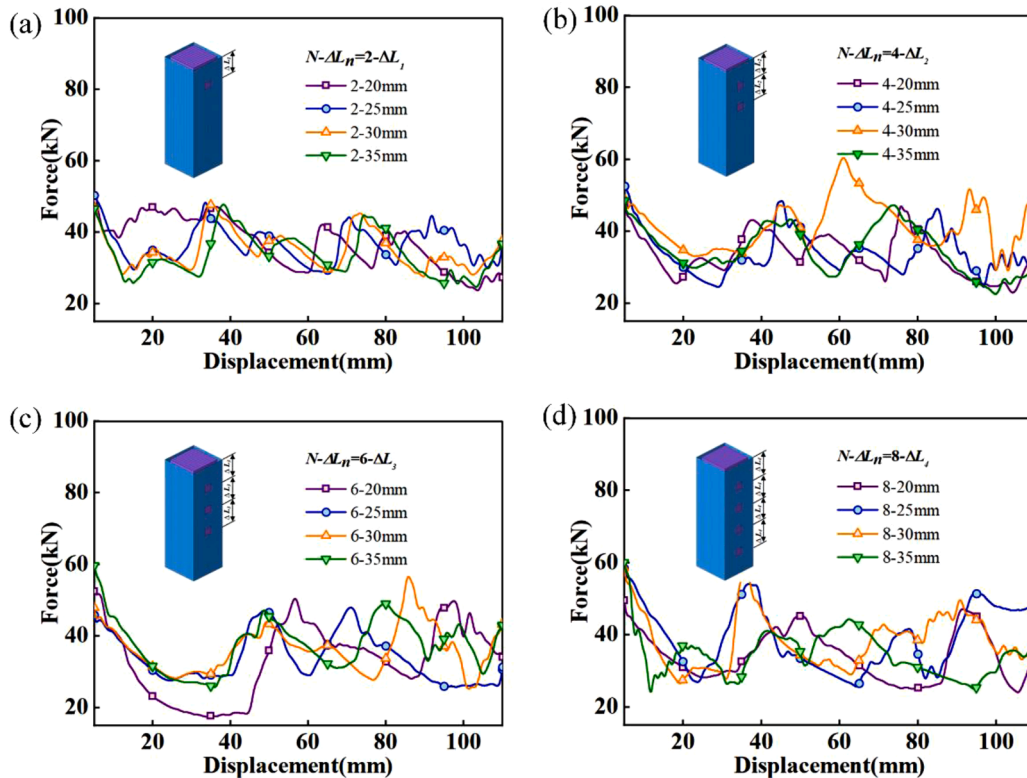
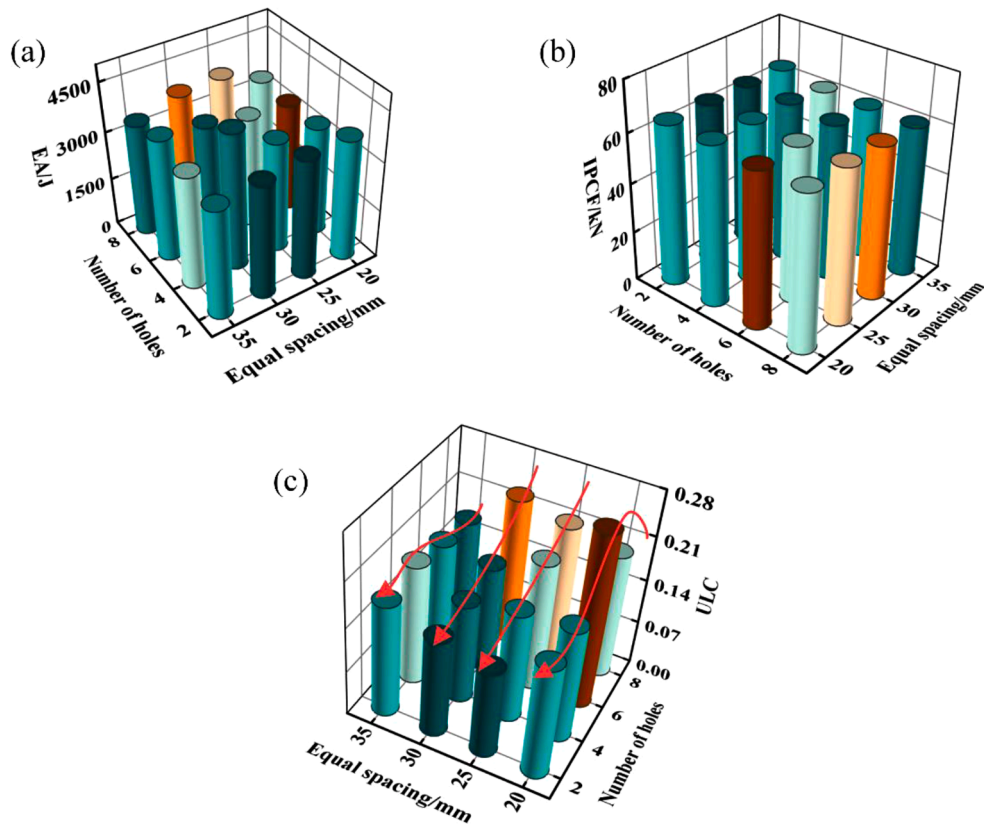


Fig. 10. Force–displacement curves of AFOTs under different numbers of holes at equal spacing including 20 mm, 25 mm, 30 mm, and 35mm: (a) Two equally spaced holes; (b) Four equally spaced holes; (c) Six equally spaced holes; (d) Eight equally spaced holes.

Table 5.

Crashworthiness indicators of AFOTs under different numbers of holes at equal spacing.

Number of holes-spacing ($N-\Delta L_n$)	EA (J)	SEA (J/g)	IPCF (kN)	MCF (kN)	CFE (%)	ULC	Deformation mode
2–20 mm	3732	18.31	65.00	33.93	52.20	0.176	Symmetric
2–25 mm	3686	18.09	65.04	33.51	51.52	0.136	Symmetric
2–30 mm	3504	17.19	64.56	31.85	49.33	0.152	Symmetric
2–35 mm	3376	16.57	64.99	30.69	47.22	0.176	Symmetric
4–20 mm	3355	16.54	64.63	30.50	47.19	0.178	Symmetric
4–25 mm	3419	16.86	64.58	31.08	48.13	0.172	Symmetric
4–30 mm	4222	20.82	64.63	38.38	59.38	0.156	Symmetric
4–35 mm	3499	17.25	62.31	31.81	51.05	0.188	Symmetric
6–20 mm	3343	16.57	62.72	30.39	48.45	0.274	Mixed
6–25 mm	3409	16.89	63.07	30.99	49.14	0.201	Symmetric
6–30 mm	3663	18.15	63.16	33.30	52.72	0.167	Symmetric
6–35 mm	3787	18.77	61.82	34.43	55.69	0.176	Symmetric
8–20 mm	3436	17.11	62.59	31.24	49.91	0.197	Symmetric
8–25 mm	3962	19.73	62.89	36.02	57.27	0.214	Symmetric
8–30 mm	3894	19.39	62.20	35.40	56.91	0.230	Symmetric
8–35 mm	3483	17.35	61.37	31.66	51.59	0.169	Symmetric

**Fig. 11.** Histograms for (a) EA, (b) IPCF and (c) ULC of AFOTs under different numbers of holes at equal spacing including 20 mm, 25 mm, 30 mm, and 35 mm.

12×12 (all dimensions mm) were introduced for numerical simulation, to calculate crashworthiness indicators of the AFOTs with different sizes of square holes (Table 4). Based on deformation modes, the AFOTs with different hole sizes still show the symmetric deformation mode. Densification degrees of AFOTs with different sizes of square holes are same and a densification stage begins to be formed at 110 mm. Except for the case with a hole area of $6 \text{ mm} \times 6 \text{ mm}$, with the increase of the hole size, the IPCF, SEA, and MCF of the AFOT structure decrease, while the effects of the hole size are not obvious. On the premise of meeting EA and IPCF, a hole measuring $10 \text{ mm} \times 10 \text{ mm}$ was selected as a parameter for the follow-up study.

3.2. Effects of the number of holes and equal hole spacing

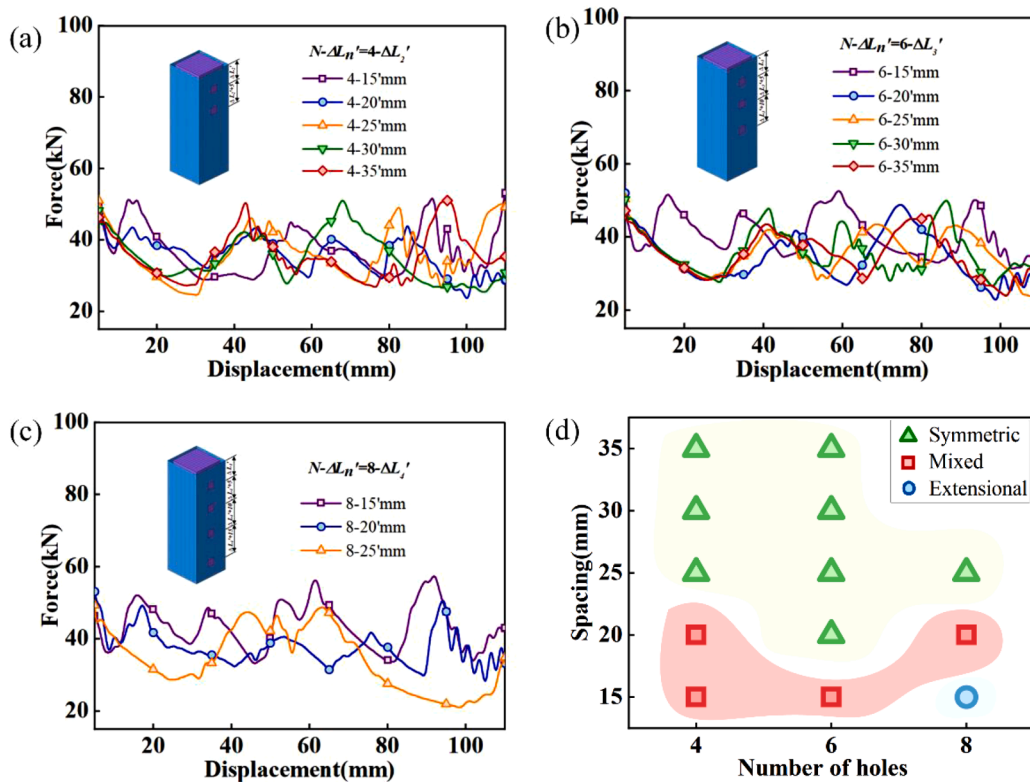
Effects of different numbers and spacings of holes on axial compression characteristics of the AFOT structure were determined. The number of holes is $2 \leq N \leq 8$ (two square holes are added each time) and the spacing between holes is $20 \text{ mm} \leq \Delta L_n \leq 35 \text{ mm}$ (a 5-mm increment is applied each time). The holes are distributed on tubes in the equal spacing. The main EA interval ranging from 5 mm to 110 mm on force-displacement curves is selected for analysis, and the numerical simulation results are demonstrated in Fig. 10 and Table 5.

By observing force-displacement curves of AFOTs under different numbers of holes with the equal spacing, the first wave crests are found to be coincided. As the number of holes increases, the subsequent wave crests and troughs are more dispersed. Meanwhile, as the spacing

Table 6.

Crashworthiness indicators of AFOTs for different numbers of holes at unequal spacings.

Number of holes-spacing ($N-\Delta L_n$)	EA (J)	SEA (J/g)	IPCF (kN)	MCF (kN)	CFE (%)	ULC	Deformation mode
4-15' mm	3741	18.45	63.57	34.01	53.50	0.167	Mixed
4-20' mm	3599	17.75	63.28	32.72	51.71	0.135	Mixed
4-25' mm	3631	17.90	62.69	33.01	52.66	0.180	Symmetric
4-30' mm	3527	17.39	61.85	32.06	51.84	0.189	Symmetric
4-35' mm	3567	17.59	61.48	32.43	52.75	0.173	Symmetric
6-15' mm	4094	20.29	62.03	37.22	60.00	0.140	Mixed
6-20' mm	3446	17.08	61.85	31.33	50.65	0.192	Symmetric
6-25' mm	3596	17.82	61.65	32.69	53.03	0.156	Symmetric
6-30' mm	3618	17.93	60.95	32.89	53.96	0.165	Symmetric
6-35' mm	3528	17.48	60.27	32.07	53.21	0.167	Symmetric
8-15' mm	4385	21.84	61.43	39.86	64.89	0.136	Extensional
8-20' mm	3792	18.88	61.21	34.47	56.31	0.125	Mixed
8-25' mm	3454	17.20	61.08	31.40	51.41	0.241	Symmetric

**Fig. 12.** Force–displacement curves for different numbers of holes at unequal spacings including 15 mm, 20 mm, 25 mm, 30 mm, and 35mm: (a) Four unequally spaced holes; (b) Six unequally spaced holes; (c) Eight unequally spaced holes; (d) Distribution of deformation modes.

between holes increases, the phase lag of the second and third wave crests increases, that is, the range of distribution of subsequent wave crests expands. For example, for the AFOT with six square holes at equal spacing, the first and second wave crests and troughs are distributed at displacements of 5 and 50 mm and the third wave crests are present at 97.6, 70.9, 85.9, and 80.5 mm. The difference between the maximum spacing and minimum spacing is 15 mm and the range of distribution of the third wave crests reaches 26.7 mm, which is 1.8 times that of the difference in spacings. By comparing deformation modes of AFOTs under different numbers of holes with different equal spacings, AFOTs mostly demonstrate the symmetric deformation mode. However, the mixed-deformation mode appears for 6 holes at 20 mm. The reason is that, at an equal spacing of 20 mm, the spacing between edges of two square holes is smaller than the fold half-wavelength, and the structural strength at square holes is smaller than that near the location without holes. Therefore, collapse occurs between upper and lower edges of two

adjacent square holes and the mixed-deformation mode finally appears.

EA, IPCF, and ULC in Table 5 are selected for comparison, and the corresponding histograms are shown in Fig. 11. For EA, the number of holes and equal spacing have little effect and the value of EA fluctuates within a certain range. At partial equal spacing, IPCF decreases as the number of holes increases. Meanwhile, with the increase in the number of holes, ULC generally shows a decreasing trend, therefore, when the number of holes increases, the value of IPCF may decrease, while the stability of the AFOT may decrease.

3.3. Effects of the number of holes and unequal hole spacing

The equal spacing between square holes is replaced by holes at unequal spacings that are in an arithmetic sequence with a variance of 5 mm and the spacing between holes is $15 \text{ mm} \leq \Delta L_n' \leq 35 \text{ mm}$ (in 5-mm increments). For instance, $\Delta L_2' = 15 \text{ mm}$ represents 15 mm from the first

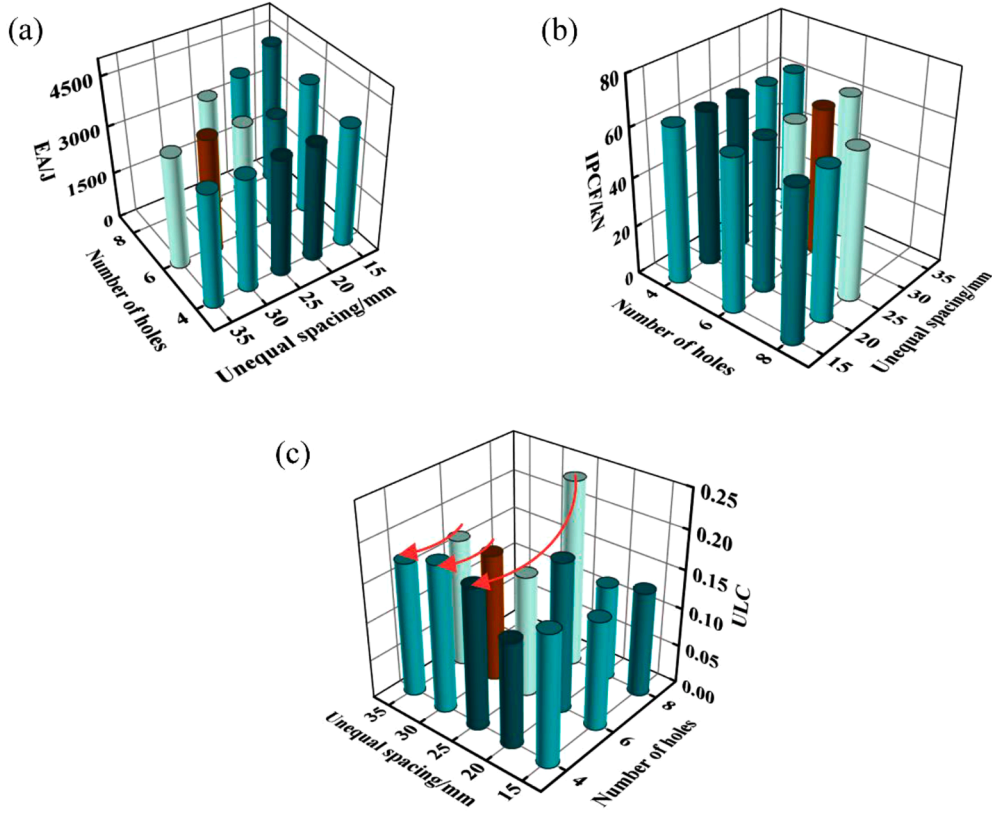


Fig. 13. Histograms for (a) EA, (b) IPCF, and (c) ULC of AFOTs under different numbers of holes at unequal spacing including 15 mm, 20 mm, 25 mm, 30 mm, and 35 mm.

square hole to the top (the distance from the second hole to the first square hole is 20 mm), as shown in Table 6. The numerical simulation results are illustrated in Fig. 12.

Wave crests and troughs on force–displacement curves are more

dispersed compared with those under the equal spacing, which are manifested as greater dislocation of phases of other wave crests on corresponding curves except for phases of the first wave crest. Under the smaller spacing between holes ($\Delta L_2' = 15$ and 20 mm, $\Delta L_3' = 15$ mm and

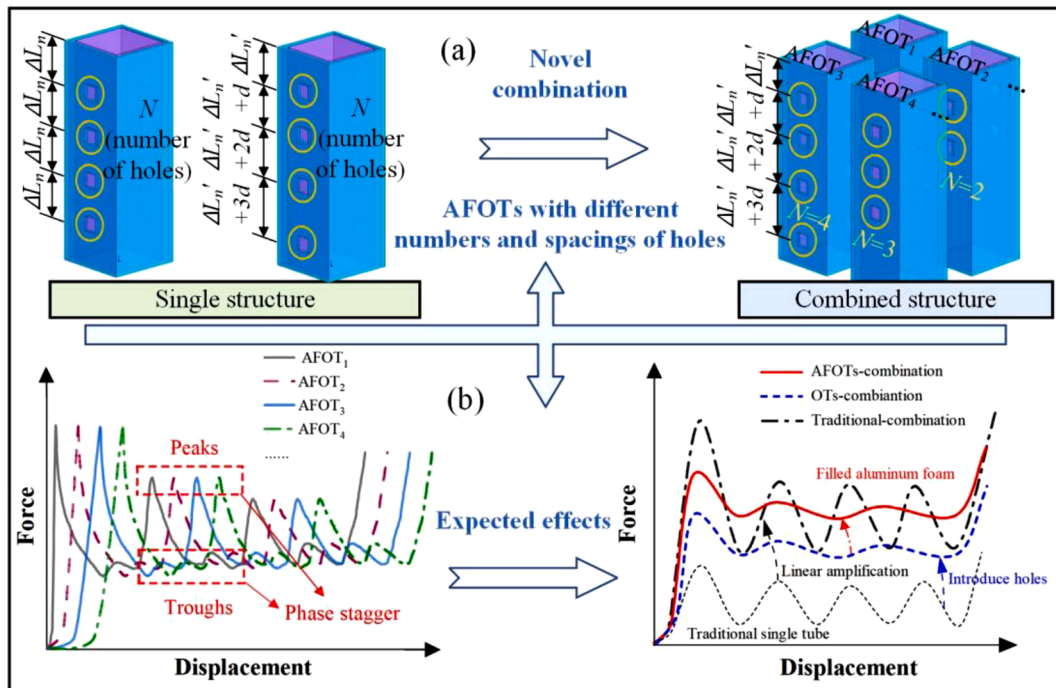


Fig. 14. AFOTs Combination with different numbers and spacings of holes and expected effects: (a) Schematic diagram of different amount of AFOT structures; (b) Force-displacement effect diagram of different amount of AFOT combination.

Table 7.

Crashworthiness indicators of AFOTs under different spacings between holes.

Combination of categories	Specific combination($N\Delta L_n / N\Delta L_n'$)	EA (J)	SEA (J/g)	IPCF (kN)	MCF (kN)	CFE (%)	ULC
Equal spacing	2–20 mm + 6–35 mm	7407	18.26	123.76	67.34	54.41	0.118
	2–20 mm + 6–35 mm	7215	17.79	124.81	65.59	52.55	0.133
	2–25 mm + 6–30 mm	7362	18.15	127.07	66.93	52.67	0.113
	2–25 mm + 6–35 mm	7377	18.19	124.98	67.06	53.66	0.133
Unequal spacing	2–25 mm + 4–30' mm	7186	17.67	126.09	65.33	51.81	0.100
	4–30' mm + 8–20' mm	7344	18.20	122.39	66.76	54.55	0.109
	6–25' mm + 8–20' mm	7486	18.59	122.84	68.05	55.40	0.115
	6–30' mm + 8–20' mm	7452	18.51	122.05	67.75	55.51	0.138

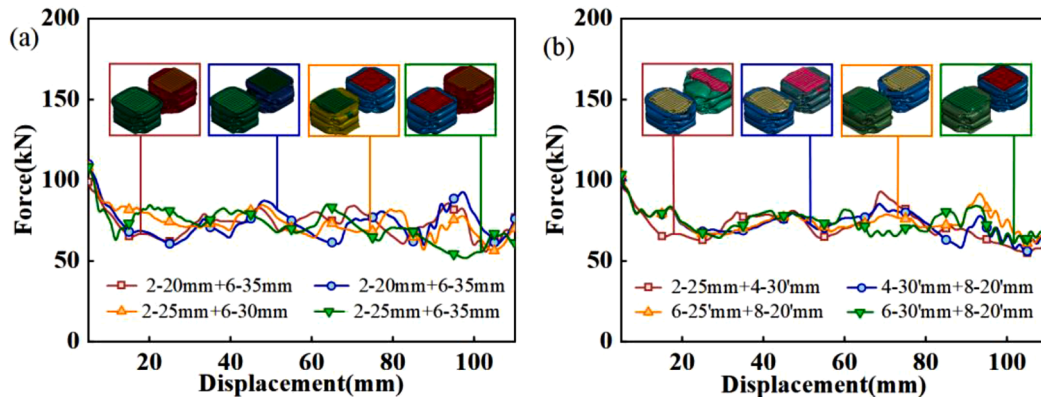


Fig. 15. Force–displacement curves of the two-AFOT combined structures: (a) Two-AFOT combined structure under an equal spacing (2–20mm+6–35 mm, 2–20mm+6–35 mm, 2–25mm+6–30 mm, and 2–25mm+6–35 mm); (b) Two-AFOT combined structure under an unequal spacing (2–25mm+4–30mm, 4–30mm+8–20mm, 6–25mm+8–20mm, and 6–30mm+8–20mm).

$\Delta L_4' = 15$ and 20 mm), the first wave crest is followed by a smaller wave crest, because the mode of deformation of the structure changes. For example, under the condition of unequally spaced eight square holes, namely $\Delta L_4' = 15$ mm, it is difficult to form a collapse mechanism in the axial compression due to the small spacing of the first hole, so extensional deformation occurs. The symmetric deformation mode appears under the other conditions. Therefore, as the spacing of the first hole increases, the deformation mode of AFOTs changes in the sequence of extensional, mixed and symmetric modes. The distribution of deformation modes is shown in Fig. 12(d). As demonstrated in Table 6, the EA and CFE are 4385 J and 64.89% under the extensional deformation mode when $\Delta L_4' = 15$ mm. In comparison with the mixed-deformation mode and symmetric deformation mode in the same group, the EA is increased by 15.64% and 26.95% and the CFE is increased by 15.24% and 26.22%, respectively. The EA efficiency and CFE under the extensional deformation mode are the highest, followed by those under the mixed-deformation mode, while the minimum values are found under symmetrical deformation.

A comparison of EA, IPCF, and ULC at unequal spacing is shown in Fig. 13; the higher EA is concentrated at the larger spacing, and the highest EA is 8–15 mm (at a value of 4385 J). The initial peak force is similar. For ULC, when the unequal spacing is large, ULC increases gradually with the increase in the number of holes, which is consistent with the phenomenon described in Section 3.2.

Under different modes of deformation, the collapse preferentially occurs at holes. The initiator of square holes reduces the structural strength and stress is readily concentrated there under axial compressive force. This finding suggests that square holes can induce deformation of the structure in the specified location and the spacing between holes affects the phase distribution of wave crests and troughs on force–displacement curves.

3.4. Axial compression characteristics of the structure combining multiple AFOTs

A single AFOT still shows an obvious peak load and load fluctuation. If multiple tubes are simply combined, the peak value and load fluctuation of the whole structure will be amplified, which is contrary to the original design intention of the energy-absorbing structure. Therefore, for the phenomena described in Sections 3.2 and 3.3, AFOTs with obvious phase differences under different numbers and spacings of holes are combined to offset peak and valley values on force–displacement curves. A collaborative innovation combination mode based on AFOTs with different numbers and spacings of holes was proposed and compared with traditional linear stacked thin-walled tubes. The combination and expected effect of different numbers and spacings of holes are shown in Fig. 14. Fig. 14(a) shows the composite structure of AFOT with different numbers and spacings of holes, and Fig. 14(b) shows the expected effect diagram before and after combination. Moreover, the stationarity of the structure was evaluated based on the ULC.

3.4.1. Two-AFOT combined structure

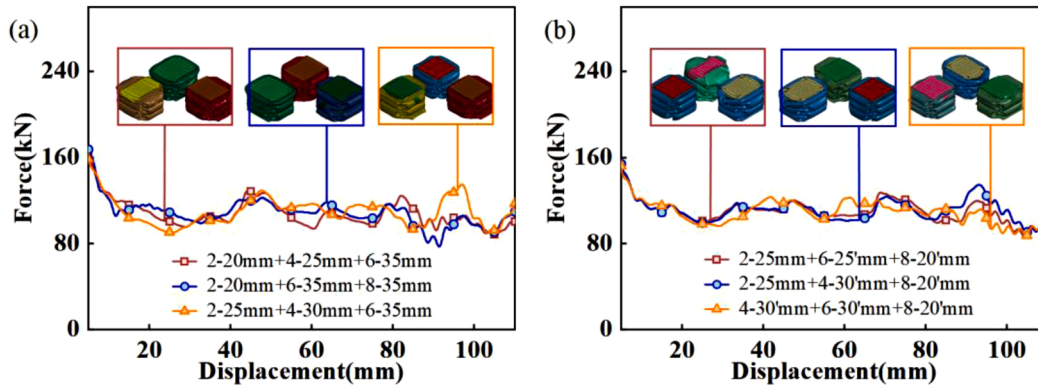
Under the equal spacing and unequal spacing in Sections 3.2 and 3.3, AFOTs with representative phase deviations on force–displacement curves and excellent crashworthiness were combined, as shown in Table 7. The force–displacement curves in Fig. 15 were also obtained.

The fluctuations in load of the two-AFOT combined structure are less than those of the single AFOTs; because of more obvious phase differences of AFOTs under an unequal spacing, the ULC is smaller than that of the combined structure with holes at equal spacings. After the combination, more peak and valley values are offset, and the SEA remains unchanged compared with that before combination. Meanwhile, the EA and MCF increase, the ULC value of the combined structure 4–30 mm + 8–20 mm is reduced by 42.33% and 12.8% and the MCF is increased by 108.23% and 93.68% compared with the single AFOTs before

Table 8.

Crashworthiness indicators of three-AFOT combined structures at different spacings.

Combination of categories	Specific combination($N\Delta L_n / N\Delta L_n'$)	EA (J)	SEA (J/g)	IPCF (kN)	MCF (kN)	CFE (%)	ULC
Equal spacing	2–20 mm + 4–25 mm + 6–35 mm	10,832	17.80	203.98	98.47	48.27	0.126
	2–20 mm + 6–35 mm + 8–35 mm	10,905	17.98	200.37	99.14	49.48	0.110
	2–25 mm + 4–30 mm + 6–35 mm	11,043	18.15	203.65	100.39	49.30	0.122
Unequal spacing	2–25 mm + 6–25' mm + 8–20' mm	11,205	18.48	201.56	101.86	50.54	0.101
	2–25 mm + 4–30' mm + 8–20' mm	11,065	18.22	201.95	100.59	49.81	0.101
	4–30' mm + 6–30' mm + 8–20' mm	11,003	18.17	199.12	100.03	50.24	0.106

**Fig. 16.** Force–displacement curves of three-AFOT combined structures: (a)Three-AFOT combined structure under an equal spacing (2–20mm+4–25mm+6–35 mm, 2–20mm+6–35mm+8–35 mm, and 2–25mm+4–30mm+6–35 mm); (b) Three-AFOT combined structure under an unequal spacing (2–25mm+6–25mm+8–20mm, 2–25mm+4–30mm+8–20mm, and 4–30mm+6–30mm+8–20mm).**Table 9.**

Crashworthiness indicators of four-AFOT structures at different spacings.

Combination of categories	Specific combination($N\Delta L_n / N\Delta L_n'$)	EA (J)	SEA (J/g)	IPCF (kN)	MCF (kN)	CFE (%)	ULC
Equal spacing	2–20 mm + 4–25 mm + 6–35 mm + 8–35 mm	14,349	17.73	263.98	130.45	49.42	0.115
	2–25 mm + 4–30 mm + 6–35 mm + 8–20 mm	14,619	18.07	265.29	132.90	50.10	0.136
Unequal spacing	2–25 mm + 4–30' mm + 6–20' mm + 8–20' mm	14,460	17.87	263.73	131.45	49.84	0.117
	2–25 mm + 4–30' mm + 6–30' mm + 8–20' mm	14,612	18.06	262.78	132.84	50.55	0.098
	4–30' mm + 6–30' mm + 8–20' mm						

combination.

By combining AFOTs with different phase differences, the amplitudes of the peaks and valleys can be offset while ensuring the SEA, but only part of fluctuation can be offset for the two-AFOT combined structure. Therefore, the stationarity of EA of the three-AFOT combined structure was further evaluated by increasing the number of AFOTs in the combined energy-absorbing structure.

3.4.2. Three-AFOT combined structure

The three-AFOT combined structure was studied by adding another AFOT with other phase differences, as listed in Table 8 and force–displacement curves in Fig. 16 were obtained. Forces applied by a loading platen are uniformly distributed on the bearing surface of the structure and the combination of single tubes does not affect the deformation mode of the structure. Similarly, the ULC of the three-AFOT combined structure under an unequal spacing is smaller than that under the equal spacing overall. By comparing crashworthiness indicators before and after combination, the EA and MCF increase significantly. Moreover, the stationarity index CFE increases to a certain extent, while the ULC further decreases. For instance, the ULC value of the combined structure (2–25 mm + 6–25mm + 8–20mm) with the best performance is decreased by 25.74%, 35.26%, and 19.20%, while the MCF is

increased by 203.97%, 211.59%, and 195.50% compared separately with individual AFOTs before combination. The EA and its stationarity of the structure are thus improved.

By comparing data in Tables 7 and 8, the stationarity of EA of most three-AFOT combined structures increases to some extent in comparison with the two-AFOT combined structure. For example, the SEA of the three-AFOT combined structure (4–30mm + 6–30mm + 8–20mm) after adding the tube (4–30mm) slightly decreases, while the ULC of the structure decreases from 0.138 to 0.106. Therefore, the further addition of a tube in the combination does not influence the SEA of the structure but does improve the stationarity of EA of the structure to a certain extent.

3.4.3. Four-AFOT combined structure

The four-AFOT combined structures with obvious phase differences were selected for numerical simulation, thus obtaining the results listed in Table 9. To improve the stationarity of the combined structure, the optimal four-AFOT combined structure (2–25 mm + 4–30mm + 6–30mm + 8–20mm) was selected. The individual four tubes before combination subjected to four-fold linear superposition and the combined structure were placed in the same coordinate system to plot their force–displacement curves (Fig. 17(a)). The ULC value of the combined

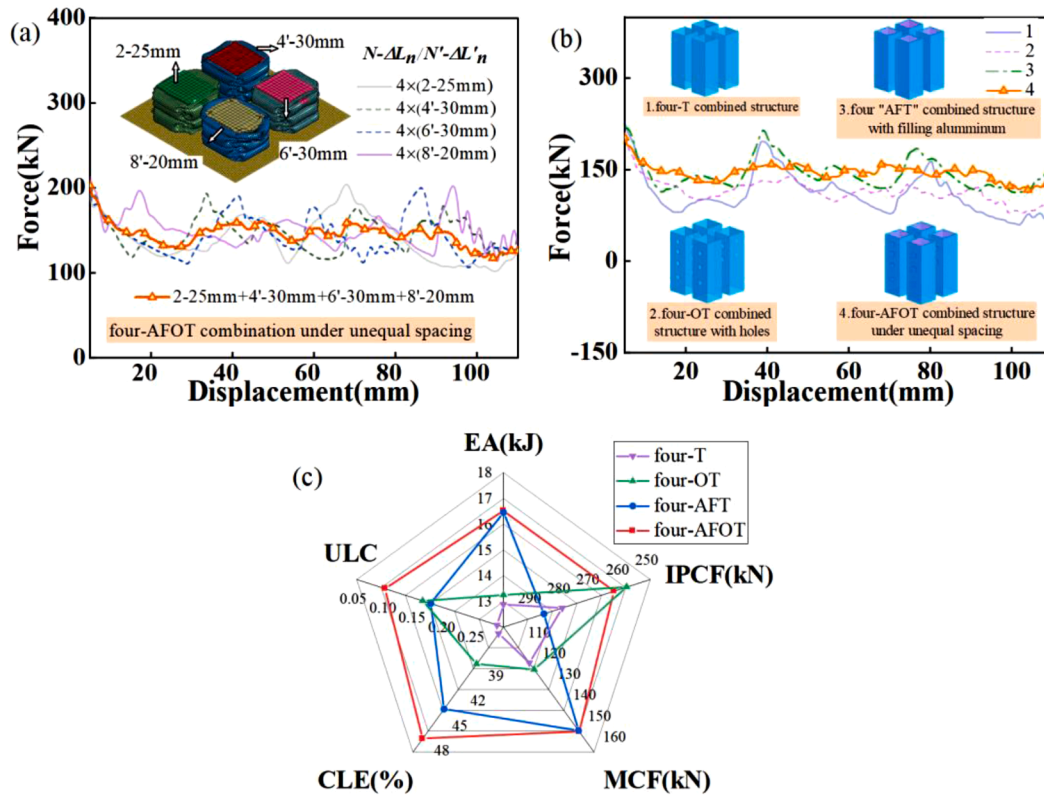


Fig. 17. Four-AFOT combined structure: (a) Force–displacement curves of the four-AFOT combined structures under $4 \times (2-25 \text{ mm}, 4-30' \text{ mm}, 6-30' \text{ mm}, 8-20' \text{ mm})$ and $2-25 \text{ mm} + 4-30' \text{ mm} + 6-30' \text{ mm} + 8-20' \text{ mm}$; (b) Force–displacement curves of four-tube combined structures, namely four-T, four-OT, four-AFT, and four-AFOT ($2-25 \text{ mm} + 4-30' \text{ mm} + 6-30' \text{ mm} + 8-20' \text{ mm}$) combined structures; (c) Radar plot for the four-T, four-OT, four-AFT, and four-AFOT ($2-25 \text{ mm} + 4-30' \text{ mm} + 6-30' \text{ mm} + 8-20' \text{ mm}$) combined structures.

structure is reduced by 27.94%, 8.15%, 40.61%, and 21.60%, while the MCF value is increased by 296.83%, 312.65%, 303.44%, and 287.00% separately compared with those of the structures before combination. Therefore, the four-AFOT structure increases the crashworthiness of the structure. the four-T combined structure with no aluminum foam and no holes, the four-OT combined structure with no aluminum foam and holes, and the four-AFT combined structure with aluminum foam and no holes were added for numerical simulation. Then, the force–displacement curves were obtained (Fig. 17(b)). By comparing indices for crashworthiness of the four structures, the radar diagram is plotted (Fig. 17(c)): the structures have advantages in terms of indices, such as the IPCF, MCF, CFE, and ULC. The MCF of the four-AFOT combined structure is increased by 28.11% at most, the IPCF is decreased by 7.46% at most and the ULC characterizing the stationarity of the structure is decreased by 66.09% at most.

Based on combined AFOT structures, the combination according to the sequence of peak and valley values of the structures under control of the number and spacing of square holes can reduce the load fluctuation of the structure in EA. Moreover, the stationarity of the structure increases significantly. This provides an effective design concept for a new energy-absorbing structure.

4. Conclusion

The effects of crush initiators (square holes) on axial compression characteristics of AFTs were studied through experiment and numerical simulation. The AFOTs with obvious phase differences under different numbers and spacings of holes were combined and designed. The following conclusions were reached:

Under quasi-static axial compression force, the introduction of square holes can reduce the IPCF of thin-walled tubes, but the reduced

IPCF does not decrease exponentially with the increase in the number of holes (the use of square holes is not therefore a case of “the more the better”). Filled aluminum foam makes efficient use of the thin-walled tube space and improves EA. Crush initiators in the form of square holes can induce the collapse of the structure in the specified location.

Hole parameters affect the mode of deformation of different AFOTs; AFOTs with different numbers of holes in the unequal spacing show different modes of deformation. Different numbers and spacings of holes can stagger the force–displacement curves on the wave trough phase, and unequal spacing exerts greater influences thereon. For an aluminum foam-filled tube with eight square holes, its mode of deformation changes regularly with the spacing of the holes. With the increase in the spacing of the first hole, AFOTs deform in the sequence of extensional, mixed, and symmetric modes.

A collaborative innovation combination mode based on AFOTs with different numbers and spacings of holes was proposed and compared with traditional linear stacked thin-walled tubes. The ULC of the combined structure is much smaller than those of single AFOTs before combination. In this way, the peak and valley values on force–displacement curves are offset to form a stable platform stage. The new and steady energy-absorbing structure, namely the four-AFOT combined structure was proposed in the study of combined structures with different numbers of AFOTs. Its ULC reduces to 0.098. Compared with the four-T, four-OT, and four-AFT combined structures, the MCF of the four-AFOT combined structure is increased by 28.11% at most, the IPCF is decreased by 7.46% at most and the ULC for characterizing the stationarity of the structure is reduced by 66.09%.

CRedit authorship contribution statement

Suchao Xie: Conceptualization, Methodology, Writing – original

draft, Funding acquisition. **Jing Zhang**: Data curation, Writing – original draft. **Xiang Liu**: Visualization, Investigation. **Shiwei Zheng**: Formal analysis, Writing – review & editing. **Zinan Liu**: Validation.

Declaration of Competing Interest

The authors declare that they have no known competing financial interests or personal relationships that could have appeared to influence the work reported in this paper.

Acknowledgment

Funding: This research was undertaken at Key Laboratory of Traffic Safety on Track (Central South University), Ministry of Education, China. The authors gratefully acknowledge the support from the National Natural Science Foundation of China [Grant No. 51775558]. This paper also supported by the Nature Science Foundation for Excellent Youth Scholars of Hunan Province [Grant No. 2019JJ30034] and the Shenghua Yu-ying Talents Program of the Central South University (Principle Investigator: Pro. Suchao Xie).

References

- Ma W, Li Z, Xie S. Crashworthiness analysis of thin-walled bio-inspired multi-cell corrugated tubes under quasi-static axial loading. *Eng Struct* 2020;204:110069.
- Xie S, Chen P, Wang N, Wang J, Du X. Crashworthiness study of circular tubes subjected to radial extrusion under quasi-static loading. *Int J Mech Sci* 2021;192:106128.
- Xie S, Yang W, Wang N, Li H. Crashworthiness analysis of multi-cell square tubes under axial loads. *Int J Mech Sci* 2017;121:106–18.
- Gao GJ, Zhuo TY, Guan WY. Recent research development of energy-absorption structure and application for railway vehicles. *J Cent South Univ* 2020;27:1012–38.
- Xing J, Xu P, Zhao H, Yao SG, Wang QX, Li BH. Crashworthiness design and experimental validation of a novel collision post structure for subway cab cars. *J Cent South Univ* 2020;27:2763–75.
- Wang S, Peng Y, Wang T, Che Q, Xu P. Collision performance and multi-objective robust optimization of a combined multi-cell thin-walled structure for high speed train. *Thin Walled Struct* 2019;135:341–55.
- Yang X, Ma J, Wen D, Yang J. Crashworthy design and energy absorption mechanisms for helicopter structures: a systematic literature review. *Prog Aerosp Sci* 2020;114:100618.
- Ahmad Z, Thambiratnam DP. Application of foam-filled conical tubes in enhancing the crashworthiness performance of vehicle protective structures. *Int J Crashworthiness* 2009;14:349–63.
- Dolzyk G, Jung S, Ufodike CO. Crashworthiness of circular tubes with rhombus star grooving pattern. *Mater Today Commun* 2021;29:102899.
- Zhou C, Ming S, Xia C, Wang B, Bi X, Hao P, Ren M. The energy absorption of rectangular and slotted windowed tubes under axial crushing. *Int J Mech Sci* 2018;141:89–100.
- Singh SK, Pandey R, Upadhyay A. A numerical study on combined effects of groove shape and numbers on crashworthiness characteristics of thin-walled tube. *Mater Today Proc* 2021;44:4381–6.
- Tran T. Study on the crashworthiness of windowed multi-cell square tubes under axial and oblique impact. *Thin Walled Struct* 2020;155:106907.
- Nikkhah H, Guo F, Chew Y, Bai J, Song J, Wang P. The effect of different shapes of holes on the crushing characteristics of aluminum square windowed tubes under dynamic axial loading. *Thin Walled Struct* 2017;119:412–20.
- Kathiresan M. Influence of shape, size and location of cutouts on crashworthiness performance of aluminium conical frusta under quasi-static axial compression. *Thin-Walled Struct* 2020;154:106793.
- Song J, Guo F. A comparative study on the windowed and multi-cell square tubes under axial and oblique loading. *Thin Walled Struct* 2013;66:9–14.
- Song J, Chen Y, Lu G. Axial crushing of thin-walled structures with origami patterns. *Thin-Walled Struct* 2012;54:65–71.
- Zhou C, Wang B, Ma J, You Z. Dynamic axial crushing of origami crash boxes. *Int J Mech Sci* 2016;118:1–12.
- Ciampaglia A, Fiumarella D, Boursier N, Ciardiello R, Belingardi G. Impact response of an origami-shaped composite crash box: experimental analysis and numerical optimization. *Compos Struct* 2021;256:113093.
- Baroutaji A, Sajjia M, Olabi AG. On the crashworthiness performance of thin-walled energy absorbers: recent advances and future developments. *Thin Walled Struct* 2017;118:137–63.
- Isaac CW, Ezekwem C. A review of the crashworthiness performance of energy absorbing composite structure within the context of materials, manufacturing and maintenance for sustainability. *Compos Struct* 2021;257:113081.
- Abramowicz W, Jones N. Dynamic axial crushing of square tubes. *Int J Impact Eng* 1984;2:179–208.
- Abramowicz W, Jones N. Dynamic progressive buckling of circular and square tubes. *Int J Impact Eng* 1986;4:243–70.
- Liu W, Lian J, Münstermann S, Zeng C, Fang X. Prediction of crack formation in the progressive folding of square tubes during dynamic axial crushing. *Int J Mech Sci* 2020;176:105534.
- Guillow SR, Lu G, Grzebieta RH. Quasi-static axial compression of thin-walled circular aluminium tubes. *Int J Mech Sci* 2001;43:2103–23.
- Li ZG, Yang HF, Zhang ZS, Sun Y, Han ZT, Wei JF. Crashworthiness of extruded magnesium thin-walled square tubes. *Trans Nonferrous Met Soc China* 2019;29:1223–32.
- Wang Z, Zhang J, Li Z, Shi C. On the crashworthiness of bio-inspired hexagonal prismatic tubes under axial compression. *Int J Mech Sci* 2020;186:105893.
- Chen Y, Bai Z, Zhang L, Wang Y, Sun G, Cao L. Crashworthiness analysis of octagonal multi-cell tube with functionally graded thickness under multiple loading angles. *Thin Walled Struct* 2017;110:133–9.
- Chen J, Li E, Li Q, Hou S, Han X. Crashworthiness and optimization of novel concave thin-walled tubes. *Compos Struct* 2022;283:115109.
- Marzbannad J, Ebrahimi MR. Multi-objective optimization of aluminum hollow tubes for vehicle crash energy absorption using a genetic algorithm and neural networks. *Thin Walled Struct* 2011;49:1605–15.
- Albak EI. Crashworthiness design and optimization of nested structures with a circumferentially corrugated circular outer wall and inner ribs. *Thin Walled Struct* 2021;167:108219.
- Zou X, Gao GJ, Dong HP, Li J, Zhou XS, Chen W, Guan WY. Crushing analysis and multi-objective optimization of bitubular hexagonal columns with ribs. *J Cent South Univ* 2017;24:1164–73.
- Xu P, Yang C, Peng Y, Yao S, Zhang D, Li B. Crash performance and multi-objective optimization of a gradual energy-absorbing structure for subway vehicles. *Int J Mech Sci* 2016;107:1–12.
- Bahramian N, Khalkhali A. Crashworthiness topology optimization of thin-walled square tubes, using modified bidirectional evolutionary structural optimization approach. *Thin-Walled Struct* 2020;147:106524.
- Baykasoğlu A, Baykasoğlu C, Cetin E. Multi-objective crashworthiness optimization of lattice structure filled thin-walled tubes. *Thin Walled Struct* 2020;149:106630.
- Patel V, Tiwari G, Dumpala R. Crashworthiness analysis of multi-configuration thin walled co-axial frusta tube structures under quasi-static loading. *Thin Walled Struct* 2020;154:106872.
- Cho YB, Bae CH, Suh MW, Sin HC. A vehicle front frame crash design optimization using hole-type and dent-type crush initiator. *Thin Walled Struct* 2006;44:415–28.
- Bodlani SB, Kim YSC, Nurick GN. The energy absorption characteristics of square mild steel tubes with multiple induced circular hole discontinuities—part I: experiments. *J Appl Mech* 2009;76:3114971.
- Bodlani SB, Kim YSC, Nurick GN. The energy absorption characteristics of square mild steel tubes with multiple induced circular hole discontinuities—part II: numerical simulations. *J Appl Mech* 2009;76:3114967.
- Li Z, Rakheja S, Shanguan WB. Study on crushing behaviors of foam-filled thin-walled square tubes with different types and number of initiators under multiple angle loads. *Thin Walled Struct* 2019;145:106376.
- Kathiresan M. Influence of shape, size and location of cutouts on crashworthiness performance of aluminium conical frusta under quasi-static axial compression. *Thin Walled Struct* 2020;154:106793.
- Kim JH, Cho DH, Choi SU, Cho CH, Kim KH. Energy absorption of square tubes with perforations in dynamic axial crush. *Int J Precis Eng Manuf* 2021;22:567–77.
- Hussein RD, Ruan D, Lu G, Thomson R. An energy dissipating mechanism for crushing square aluminium/CFRP tubes. *Compos Struct* 2018;183:643–53.
- Hassanli F, Paydar MH. Improvement in energy absorption properties of aluminum foams by designing pore-density distribution. *J Mater Res Technol* 2021;14:609–19.
- Pirmohammad S, Ahmadi-Saravani S, Zakavi S J. Crashworthiness optimization design of foam-filled tapered decagonal structures subjected to axial and oblique impacts. *J Cent South Univ* 2019;26:2729–45.
- Liu X, Zhang J, Fang Q, Wu H, Zhang Y. Response of closed-cell aluminum foams under static and impact loading: experimental and mesoscopic numerical analysis. *Int J Impact Eng* 2017;110:382–94.
- Yang X, Feng X, An T, Yang K, Sha J, Zhao N, Zong R. Investigation on microstructures, compressive properties and energy absorption capacity of carbon nanotubes/aluminum composite foam-filled tubes. *Compos Struct* 2022;282:115024.
- Duarte I, Vesjenak M, Krstulović-Opara L. Dynamic and quasi-static bending behaviour of thin-walled aluminium tubes filled with aluminium foam. *Compos Struct* 2014;109:48–56.
- Sun G, Wang Z, Yu H, Gong Z, Li Q. Experimental and numerical investigation into the crashworthiness of metal-foam-composite hybrid structures. *Compos Struct* 2019;209:535–47.
- Zhang J Z, Huang L, Li C B, Chen T, Zhang C Q. Design of a novel multi-walled tube-reinforced aluminum foam for energy absorption. *Compos Struct* 2021;276:11584.
- Seitzberger M, Rammerstorfer FG, Grading R, Degischer HP, Blaimschein M, Walch C. Experimental studies on the quasi-static axial crushing of steel columns filled with aluminium foam. *Int J Solids Struct* 2000;37:4125–47.
- Ahmad Z, Thambiratnam DP. Crushing response of foam-filled conical tubes under quasi-static axial loading. *Mater Des* 2009;30:2393–403.
- Wang L, Zhang B, Zhang J, Jiang Y, Wang W, Wu G. Deformation and energy absorption properties of cenosphere-aluminum syntactic foam-filled tubes under axial compression. *Thin Walled Struct* 2021;160:107364.

- [53] Liu Z, Huang Z, Qin Q. Experimental and theoretical investigations on lateral crushing of aluminum foam-filled circular tubes. *Compos Struct* 2017;175:19–27.
- [54] Song J, Xu S, Xu L, Zhou J, Zou M. Experimental study on the crashworthiness of bio-inspired aluminum foam-filled tubes under axial compression loading. *Thin Walled Struct* 2020;155:106937.
- [55] Gong C, Bai Z, Lv J, Zhang L. Crashworthiness analysis of bionic thin-walled tubes inspired by the evolution laws of plant stems. *Thin Walled Struct* 2020;157: 107081.
- [56] Xiang X, Zou S, Ha NS, Lu G, Kong I. Energy absorption of bio-inspired multi-layered graded foam-filled structures under axial crushing. *Compos Part B Eng* 2020;198:108216.
- [57] Yao R, Pang T, He S, Li Q, Zhang B, Sun G. A bio-inspired foam-filled multi-cell structural configuration for energy absorption. *Compos Part B Eng* 2022;282: 109801.
- [58] Haghi Kashani M, Shahsavari Alavijeh H, Akbarshahi H, Shakeri M. Bitubular square tubes with different arrangements under quasi-static axial compression loading. *Mater Des* 2013;51:1095–103.
- [59] Azimi MB, Asgari M. A new bi-tubular conical–circular structure for improving crushing behavior under axial and oblique impacts. *Int J Mech Sci* 2016;105: 253–65.
- [60] Goel MD. Deformation, energy absorption and crushing behavior of single-, double- and multi-wall foam filled square and circular tubes. *Thin Walled Struct* 2015;90:1–11.
- [61] Sharifi S, Shakeri M, Fakhari HE, Bodaghi M. Experimental investigation of bitubular circular energy absorbers under quasi-static axial load. *Thin Walled Struct* 2015; 89:42–53.
- [62] Xie SC, Zhou H, Liang XF, Ren X. Contrastive analysis and crashworthiness optimization of two composite thin-walled structures. *J Cent South Univ* 2014;21: 4386–94.
- [63] Goyal S, Anand CS, Sharma SK, Sharma RC. Crashworthiness analysis of foam filled star shape polygon of thin-walled structure. *Thin Walled Struct* 2019;144:106312.
- [64] Zhu G, Zhao Z, Hu P, Luo G, Zhao X, Yu Q. On energy-absorbing mechanisms and structural crashworthiness of laterally crushed thin-walled structures filled with aluminum foam and CFRP skeleton. *Thin Walled Struct* 2021;160:107390.
- [65] LS-DYNA keyword user's manual. Livermore, CA: Livermore Software Technology Corporation; 2017.
- [66] Hou S, Li Q, Long S, Yang X, Li W. Crashworthiness design for foam filled thin-wall structures. *Mater Des* 2009;30:2024–32.
- [67] Mete OH, Yalcin M, Genel K. Experimental and numerical studies on the folding response of annular-rolled Al tube. *Thin Walled Struct* 2018;127:798–808.
- [68] Chen S, Yu H, Fang J. A novel multi-cell tubal structure with circular corners for crashworthiness. *Thin-Walled Struct* 2018;122:329–43.
- [69] GB/T 228.1-2010. Metallic materials - tensile testing - part 1: method of test at room temperature. Beijing: Chinese Standard Press; 2010.
- [70] Duarte I, Krstulović-Opara L, Vesnjak M. Characterisation of aluminium alloy tubes filled with aluminium alloy integral-skin foam under axial compressive loads. *Compos Struct* 2015;121:154–62.
- [71] Duarte I, Vesnjak M, Krstulović-Opara L, Ren Z. Static and dynamic axial crush performance of *in-situ* foam-filled tubes. *Compos Struct* 2015;124:128–39.